

## Embedded Ultrasonics NDE with Piezoelectric Wafer Active Sensors

**Victor Giurgiutiu**

Department of Mechanical Engineering, University of South Carolina, Columbia, SC 29208, USA

[victorg@sc.edu](mailto:victorg@sc.edu)

---

*ABSTRACT: The use of piezoelectric wafer active sensors (PWAS) for embedded ultrasonic nondestructive evaluation (NDE) is described. PWAS structure and principle of operation are presented. The interaction between PWAS and ultrasonic Lamb waves is modeled and analyzed, and excitation "sweet spots" for preferentially exciting certain Lamb wave modes are identified. Recent trends in guided-wave ultrasonic NDE and damage identification are briefly reviewed. Then, the use of PWAS for embedded pulse-echo detection of structural cracks is exemplified. For large area interrogation, PWAS phased arrays are used in conjunction with the embedded ultrasonics structural radar (EUSR) algorithm to create scanning Lamb wave beams. For local area interrogation, the use of PWAS in conjunction with the electromechanical (E/M) impedance method is discussed with examples of local area crack detection in circular plates and aircraft panels. Spectral classification methods based on overall statistics and neural networks are discussed. Passive PWAS usage for acoustic emission and impact detection is presented. The use of PWAS for Rayleigh wave ultrasonics is also illustrated. Finally, we evaluate the role and opportunities of PWAS as the enabling technology for large area structural health monitoring, damage detection, and embedded NDE.*

*KEYWORDS: piezoelectric, ultrasonic, NDE, PWAS, E/M impedance, acoustic emission, damage, impact detection, Lamb waves, Rayleigh waves, EUSR*

---

### **1 Introduction**

Piezoelectric wafer active sensors (PWAS) are inexpensive low-profile transducers that operate on the piezoelectric principle. Initially, PWAS were used for vibrations control, as pioneered by Crawley et al. (1987) and Fuller et al (1990). Tzou and Tseng (1990) and Lester and Lefebvre (1993) modeled the piezoelectric sensor/actuator design for dynamic measurement/control. For damage detection, Banks et al. (1996) used PZT wafers to excite a structure and then sense the free decay response. The use of PWAS for structural health monitoring and nondestructive evaluation has followed three main paths: (a) modal analysis and transfer function; (b) wave propagation; (c) electromechanical impedance. The use of PWAS for damage detection with Lamb-wave propagation was pioneered by

Chang and his coworkers (Chang, 1995, 1998, 2001; Wang and Chang, 2000; Ihn and Chang, 2002). They have studied the use of PWAS for the generation and reception of elastic waves in composite materials. Passive reception of elastic waves was used for impact detection. Pitch-catch transmission-reception of low frequency Lamb waves was used for damage detection. PWAS wave propagation was also studied by Lakshmanan and Pines (1997), Culshaw et al. (1998), Lin and Yuan (2001), Dupont et al. (2000), Osmont et al. (2000), Diamanti, Hodgkinson, and Soutis (2002). The use of PWAS for high-frequency local modal sensing with the electromechanical impedance method was pursued by Liang et al. (1994), Sun et al. (1994), Chaudhry et al. (1995), Park and Inman (2001), and others. The author and his collaborators have pursued the PWAS technology along both the electromechanical impedance and the wave propagation paths (Giurgiutiu et al., 1997-2002).

PWAS couple the electrical and mechanical effects (mechanical strain,  $S_{ij}$ , mechanical stress,  $T_{kl}$ , electrical field,  $E_k$ , and electrical displacement  $D_j$ ) through the tensorial piezoelectric constitutive equations

$$\begin{aligned} S_{ij} &= s_{ijkl}^E T_{kl} + d_{kij} E_k \\ D_j &= d_{jkl} T_{kl} + \epsilon_{jk}^T E_k \end{aligned} \quad (1)$$

where  $s_{ijkl}^E$  is the mechanical compliance of the material measured at zero electric field ( $E = 0$ ),  $\epsilon_{jk}^T$  is the dielectric permittivity measured at zero mechanical stress ( $T = 0$ ), and  $d_{kij}$  represents the piezoelectric coupling effect. As apparent in Figure 1, PWAS are small and unobtrusive. PWAS utilize the  $d_{31}$  coupling between in-plane strain and transverse electric field. A 7-mm diameter PWAS, 0.2 mm thin, weighs a bare 78 mg. At less than \$10 each, PWAS are no more expensive than conventional high-quality resistance strain gages. However, the PWAS performance exceeds by far that of conventional resistance strain gages. This is especially apparent in high frequency applications at hundreds of kHz and beyond. As shown next, PWAS can be used, in several ways.

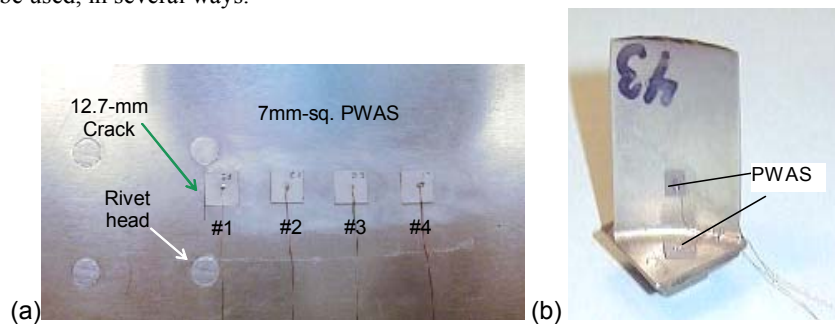


**Figure 1 Piezoelectric wafer active sensors mounted on various structures: (a) array of 7-mm square PWAS on an aircraft panel; (b) PWAS on a turbine blade**

As a high-bandwidth strain sensor, the PWAS directly converts mechanical energy to electrical energy. The conversion constant is linearly dependent on the signal frequency. In the kHz range, signals of the order of hundreds of millivolts are easily obtained. No conditioning amplifiers are needed; the PWAS can be directly connected to a high-impedance measuring instrument, such as a digitizing oscilloscope.

As a high-bandwidth strain exciter, the PWAS converts directly electrical energy into mechanical energy. Thus, it can easily induce vibrations and waves in the substrate material. It acts very well as an embedded generator of waves and vibration. High-frequency waves and vibrations are easily excited with input signals as low as 10 V. This dual sensing and excitation characteristics of PWAS justifies their name of “active sensors”.

As a resonator, PWAS undergo mechanical resonances under direct electrical excitation. Thus, very precise frequency standards can be created with a simple setup consisting of the PWAS and the signal generator. The resonant frequencies depend only on the wave speed (which is a material constant) and the geometric dimensions. Precise frequency values can be obtained through precise machining of the PWAS geometry.

As an embedded modal sensor, the PWAS is able to directly measure the high-frequency modal spectrum of a support structure. This is achieved with the electro-mechanical impedance method, which reflects the mechanical impedance of the support structure into the real part of the electromechanical impedance measured at PWAS terminals. The high-frequency characteristics of this method, which has been proven to operate at hundreds of kHz and beyond, cannot be achieved with conventional modal measurement techniques. Thus, PWAS are the sensors of choice for high-frequency modal measurement and analysis.

For nondestructive evaluation (NDE), PWAS can be used as both active and passive probes:

- 1) Far-field damage detection using pulse-echo and pitch-catch methods
- 2) Near-field damage detection using high-frequency impedance method
- 3) Acoustic emission monitoring of crack initiation and growth
- 4) Low-velocity impact detection

## 2 Guided-Wave Ultrasonic NDE and Damage Identification

Current ultrasonic inspection of thin wall structures (e.g., aircraft shells, storage tanks, large pipes, etc.) requires meticulous through-the-thickness C-scans over large areas. One method to increase the efficiency of thin-wall structures ultrasonic inspection is to utilize guided waves (e.g., Lamb waves) instead of the conventional pressure waves. As shown by Rose (1995) and Krautkramer (1998), guided waves offer the advantage of large-area coverage with a minimum of installed sensors. Guided Lamb waves propagate along the mid-surface of thin-wall plates and shallow shells and can travel at relatively large distances with very little amplitude loss (Viktorov, 1967; Rose, 1999). Similarly, Rayleigh guided waves travel at large distances over the surface of a solid object. Today’s advanced ultrasonic techniques rely on the generation, propagation, and detection of Rayleigh, Lamb, and Love waves in various structures.

One way of generating guided waves is with conventional ultrasonic transducers and wedge couplers. This can be achieved by impinging the plate obliquely with a tone-burst from a relatively large ultrasonic transducer through a wedge coupler. Snell's law ensures mode conversion at the interface, hence a combination of pressure and shear waves are simultaneously generated into the thin plate. The imposition of the tractions-free boundary conditions at the plate surfaces results in multiple reflections of these pressure and shear waves, which thus propagate along the plate. The Lamb waves result as the constructive interference of pressure and shear waves, as they propagate along the plate. Modification of the wedge angle and excitation frequency allows the selective tuning of various Lamb wave modes (Alleyne and Cawley, 1992; Rose et al., 1995). Trained personnel can find the angle of the wedge coupler, which adequately trigger the mode conversion for a particular Lamb mode. Another traditional method for selectively exciting Lamb waves is through a comb probe, in which the comb pitch is matched with the half wavelength of the targeted Lamb mode. Both the wedge and the comb probes are relatively large and expensive.

In recent year, a large number of papers have been published on the use of Lamb waves for nondestructive evaluation and damage detection (Thomson and Chimenti, 2002). Rose (2002) pointed out that the improved inspection potential of guided Lamb waves over other ultrasonic methods is due to their:

- Variable mode structure and distributions
- Multi-mode character
- Sensitivity to different type of flaws
- Propagation for long distances
- Capability to follow curvature and reach hidden and/or buried parts

Guided Lamb waves have opened new opportunities for cost-effective detection of damage in aircraft structures (Dalton, Cawley, and Lowe, 2001). The use of Lamb waves to detect the **corrosion** in aluminum structures using the **pitch-catch method** was explored by Chahbaz, *et. al.* (1999). An  $A_1$  Lamb wave mode traveling through a corroded zone ends up with a lower amplitude and longer time of flight than in a pristine zone. Experiments were performed to detect corrosion around rivets and other fasteners. The pitch-catch method was also used by Grondel et al. (1999) to assess the damage progression in a riveted aircraft splice specimen during fatigue testing. The time of flight changes were correlated with the appearance microcracks and macrocracks during fatigue testing. Alleyne et al. (2001) detected corrosion in pipes using the **pulse-echo method** using the mode conversion approach. Rose et al. (1995) used Lamb waves to detect **disbond in adhesive joints** with the pitch-catch method. In adhesive bonds, Lamb waves are able to leak from one side of the bond to the other side of the bond through "wave leakage". (In contrast, conventional ultrasonic P-waves cannot usually cross the adhesive due to impedance mismatch.) Two situations were considered: (a) lap splice joint disbonds detected as a loss of reception signal due to the signal no longer leaking across the splice; and (b) tear-strap disbond or corrosion observed as an increase of the reception signal due to the signal no longer leaking away in the tear strap. The use of Lamb waves for disbond

detection was also reported by Singher *et al.* (1997), Mustafa and Chahbaz (1997), and Todd and Challis (1999).

Guided Lamb waves have opened new opportunities for cost-effective detection of damage in aircraft structures. Light *et al.* (2001) studied the detection of defects in thin steel plates using ultrasonic guided Lamb waves and conventional ultrasonic equipment. De Villa *et al.* (2001) presented results of defect detection in thin plates using  $S_0$  Lamb wave scanning. Conventional ultrasonic equipment consisting of wedge transmitter and bubbler receiver mounted on a scanning arm was utilized. Signal processing methods for the determination of the arrival times and of the flaw location were explored. Flaw localization results for simulated cracks (notches) with various sizes (from 2 to 3.5 inches) and different inclinations (from 0 to 45 degrees) were presented. These methods can be viewed as an extension of the acousto-ultrasonic methodology (Duke, 1988). The inspection potential of ultrasonic guided wave for the detection of cracks, delaminations, and disbonds, and gave examples utilizing conventional angle-probe ultrasonic transducers have recently been outlined by Rose (2002).

These guided-wave techniques are now being transitioned to embedded active sensor applications. However, conventional Lamb-wave probes (wedge and comb transducers) are relatively too heavy and expensive to be considered for widespread deployment on an aircraft structure as part of a structural health monitoring (SHM) system. If conventional transducers were to be deployed in large numbers inside an aerospace structure, the cost and weight penalties would be exorbitant. Therefore, for structural health monitoring, a different type of Lamb wave transducer that is smaller, lighter, and cheaper than the conventional ultrasonic probes is required. Such a transducer could be deployed into the structure as sensor arrays, which would be permanently wired and interrogated at will. Thus, the opportunity for embedded ultrasonic NDE is created.

### 3 PWAS Ultrasonic Transducers

PWAS act as both Lamb-wave exciters and Lamb-wave detectors (Figure 2). PWAS couple their in-plane motion with the Lamb-waves' particle motion on the material surface. The in-plane PWAS motion is excited by the applied oscillatory voltage through the  $d_{31}$  piezoelectric coupling. Optimum excitation and detection happens when the PWAS length is an odd multiple of the half wavelength of particular Lamb wave modes. The PWAS action as ultrasonic transducers is fundamentally different from that of conventional ultrasonic transducers. Conventional ultrasonic transducers act through surface tapping, applying vibrational pressure to the object's surface. PWAS, on the other hand, act through surface pinching, and are strain coupled with the object surface. This imparts to PWAS a much better efficiency in transmitting and receiving ultrasonic Lamb and Rayleigh waves than conventional ultrasonic transducers.

PWAS are capable of geometric tuning through matching between their characteristic direction and the half wavelength of the excited Lamb mode. Rectangular shaped PWAS with high length to width ratio can generate unidirectional Lamb waves through half wavelength tuning in the length direction.

Circular PWAS excite omnidirectional Lamb waves that propagate in circular wave fronts. Unidirectional and omnidirectional Lamb wave propagation is illustrated in Figure 3. Omnidirectional Lamb waves are also generated by square PWAS, although their pattern is somehow irregular in the PWAS proximity. At far enough distance, ( $r \gg a$ ), the wave front generated by square PWAS is practically identical with that generated by circular PWAS.

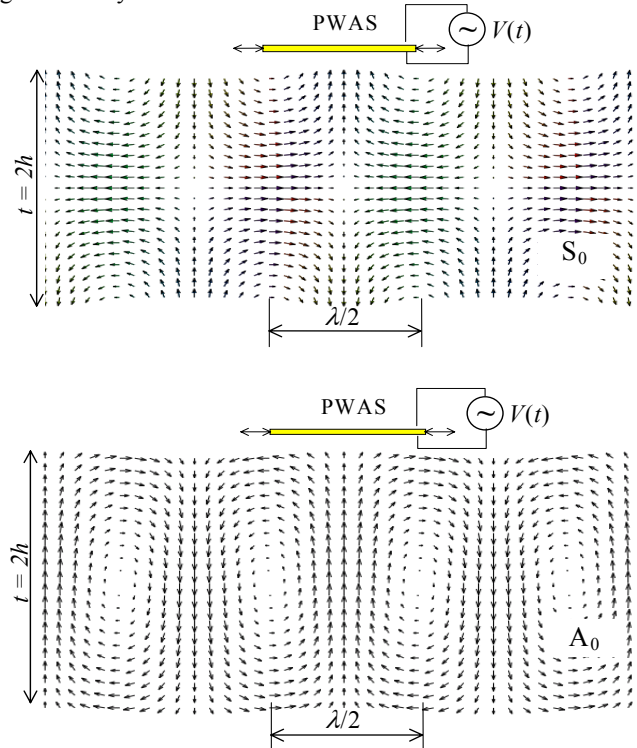


**Figure 2** The typical Lamb wave structure of the S<sub>0</sub> and A<sub>0</sub> modes highlights the conditions for optimal coupling between PWAS and Lamb waves

The operation of PWAS ultrasonic transducers is fundamentally different from that of conventional ultrasonic probes because:

- 1) PWAS achieve Lamb wave excitation and sensing through surface “pinching” (in-plane strains), while conventional ultrasonic probes excite through surface “tapping” (normal stress).
- 2) PWAS are strongly coupled with the structure and follow the structural dynamics, while conventional ultrasonic probes are relatively free from the structure and follow their own dynamics.

- 3) PWAS ultrasonic transducers are non-resonant wide-band devices, while conventional ultrasonic probes are narrow-band resonators.

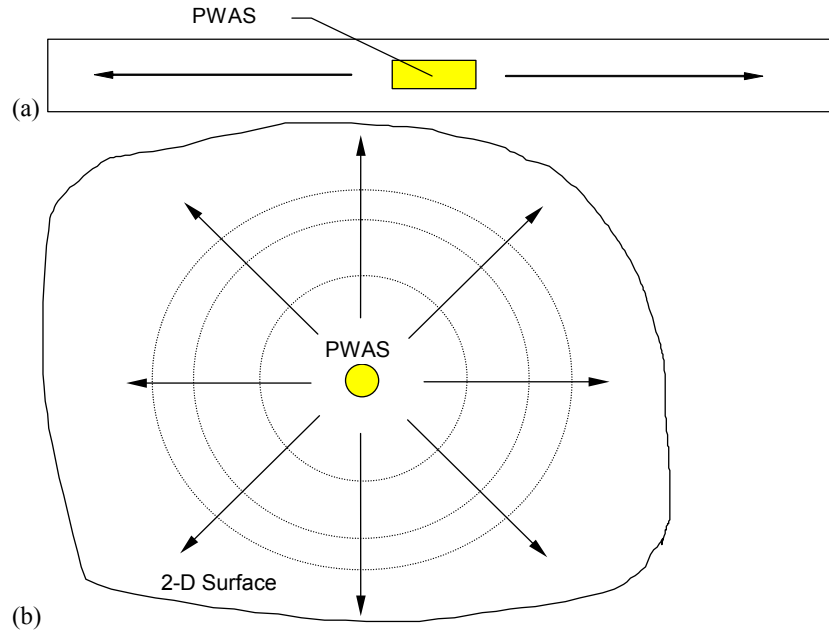


**Figure 3** (a) Elastic waves generated by a PWAS in a 1-D structure; (b) circular-crested Lamb waves generated by a PWAS in a 2-D structure

#### 4 Shear Layer Interaction between PWAS and Structure

The 1-D plane-strain analysis will be an extension of the shear-lag analysis of piezoelectric wafer excitation of thin-wall structures pioneered by Crawley and deLuis (1987) for static morphing and the quasi-static low frequency vibrations. Crawley's analysis assumes a shear-layer model of the adhesive and models the structure as a superposition of axial and flexural deformation. In Crawley's model, the Bernoulli-Euler hypothesis was applied across the plate thickness, i.e., constant displacement for axial motion, and linear displacement strain for flexural motion. Figure 4 shows a thin-wall structure of thickness  $t$  and elastic modulus  $E$ , with a PWAS of thickness  $t_a$  and elastic modulus  $E_a$  attached to its upper surface through a bonding layer of thickness  $t_b$  and shear modulus  $G_b$ . The PWAS length is  $l_a$  and half-length  $a = l_a/2$ . Upon application of an electric voltage, the PWAS experiences an induced strain  $\epsilon_{ISA} = d_{31}V/t_a$ . The induced strain is transmitted to the structure through the bonding layer interfacial shear stress  $\tau$ . Upon analysis, we obtain

$$u_a(x) = \frac{\alpha}{\alpha + \psi} \varepsilon_{ISA} a \left( \frac{x}{a} + \frac{\psi}{\alpha} \frac{\sinh \Gamma x}{(\Gamma a) \cosh \Gamma a} \right) \quad (\text{PWAS displacement}) \quad (2)$$

$$\tau(x) = \frac{t_a}{a} \frac{\psi}{\alpha + \psi} E_a \varepsilon_{ISA} \left( \Gamma a \frac{\sinh \Gamma x}{\cosh \Gamma a} \right) \quad (\text{Interfacial shear stress in bonding layer}) \quad (3)$$

$$u(x) = \frac{\alpha}{\alpha + \psi} \varepsilon_{ISA} a \left( \frac{x}{a} - \frac{\sinh \Gamma x}{(\Gamma a) \cosh \Gamma a} \right) \quad (\text{Structural displacement at the surface}) \quad (4)$$

where  $\psi = (Et)/(E_a t_a)$ , and  $\alpha$  is a parameter that depends on the stress and strain distribution across the thickness.

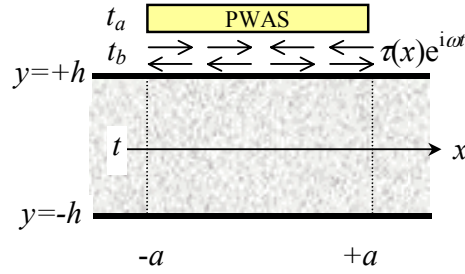


**Figure 4 Interaction between the PWAS and the structure**

Under static and low frequency dynamic conditions (i.e., uniform stress and strain for the symmetric deformation, and linear stress and strain for anti-symmetric deformation), elementary analysis yields  $\alpha = 4$ . For Lamb wave modes, which have complex stress and strain distributions across the thickness, the parameter  $\alpha$  varies from mode to mode. These equations apply for  $|x| < a$ . The shear lag parameter

$$\Gamma^2 = \frac{G_b}{E_a} \frac{1}{t_a t_b} \frac{\alpha + \psi}{\psi}$$

controls the  $x$ -distribution. The higher the  $\Gamma$ , the more localized and intense is the diffusion of stresses and strains from the PWAS into the structure. Figure 5 presents the results of our preliminary simulations of this effect on an APC-850 PWAS ( $E_a = 63$  GPa,  $t_a = 0.2$  mm,  $l_a = 7$  mm,  $d_{31} = -175$  mm/kV) bonded to a thin-wall aluminum structure ( $E = 70$  GPa and  $t = 1$  mm). The bonding layer had  $G_b = 2$  GPa. Its thickness was allowed to vary from 1  $\mu\text{m}$  to 100  $\mu\text{m}$ . It is apparent that a relatively thick bonding layer produces a slow transfer over the entire span of the PWAS (the “100  $\mu\text{m}$ ” curves in Figure 5), whereas a thin bonding layer produces a very rapid transfer (the “1  $\mu\text{m}$ ” curves in Figure 5). In this latter case, the shear stress becomes confined to the PWAS ends. This leads to the concept of **ideal bonding** (also known as the **pin-force model**), in which all the load transfer takes place over an infinitesimal region at the PWAS ends, i.e.

$$\tau(x) = a\tau_0 [\delta(x - a) - \delta(x + a)] \quad (5)$$

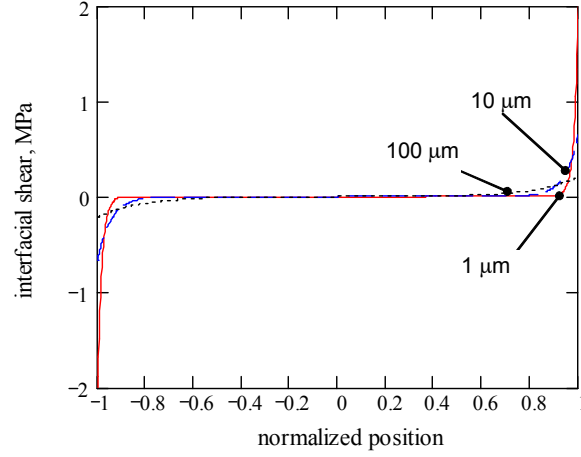


**Figure 5** Variation of shear-lag transfer mechanism with bond thickness

### 5 Tuned Excitation of Lamb Modes with PWAS transducers

The excitation of Lamb waves with PWAS transducers is studied by considering the excitation applied by the PWAS through a surface stress  $\tau = \tau_0(x)e^{i\omega t}$  applied to the upper surface of a plate in the form of shear lag adhesion stresses over the  $(-a, +a)$  interval

$$\tau_a(x) = \begin{cases} \tau_0 \sinh(\Gamma x) & |x| < a \\ 0 & \text{otherwise} \end{cases} \quad (6)$$

Applying a space-domain Fourier transform analysis of the basic Lamb wave equations yields the strain wave and displacement wave solutions in the form

$$\begin{aligned} \varepsilon_x(x, t) &= \frac{1}{2\pi} \frac{-i}{2\mu} \int_{-\infty}^{\infty} \left( \frac{\tilde{\tau} N_S}{D_S} + \frac{\tilde{\tau} N_A}{D_A} \right) e^{i(\xi x - \omega t)} d\xi \\ u_x(x, t) &= \frac{1}{2\pi} \frac{-i}{2\mu} \int_{-\infty}^{\infty} \frac{1}{\xi} \left( \frac{\tilde{\tau} N_S}{D_S} + \frac{\tilde{\tau} N_A}{D_A} \right) e^{i(\xi x - \omega t)} d\xi \end{aligned} \quad (7)$$

where  $\tilde{\tau}$  is the Fourier transform of  $\tau_a(x)$ ,  $p^2 = \frac{\omega^2}{c_L^2} - \xi^2$ ,  $q^2 = \frac{\omega^2}{c_T^2} - \xi^2$ , while

$$\begin{aligned} c_L^2 &= (\lambda + 2\mu) / \rho \quad \text{and} \quad c_T^2 = \mu / \rho \quad \text{are the longitudinal (pressure) and transverse (shear) wave speeds, } \lambda \text{ and } \mu \text{ are Lamé constants, } \rho \text{ is the mass density, and} \\ N_S &= \xi q (\xi^2 + q^2) \cos ph \cos qh, \quad D_S = (\xi^2 - q^2)^2 \cos ph \sin qh + 4\xi^2 pq \sin ph \cos qh \\ N_A &= \xi q (\xi^2 + q^2) \sin ph \sin qh, \quad D_A = (\xi^2 - q^2)^2 \sin ph \cos qh + 4\xi^2 pq \cos ph \sin qh \end{aligned} \quad (8)$$

Note that  $p$  and  $q$  depend on  $\xi$ , thus increasing the problem complexity. The integral in Equation (7) is singular at the roots of  $D_S$  and  $D_A$ . The equations  $D_S = 0$  and  $D_A = 0$  are exactly the Rayleigh-Lamb characteristic equations for symmetric and anti-symmetric motions accepting the simple roots

$$\xi_0^S, \xi_1^S, \xi_2^S, \dots \quad \xi_0^A, \xi_1^A, \xi_2^A, \dots \quad (9)$$

corresponding to the symmetric (S) and anti-symmetric (A) Lamb waveguide modes, respectively. The evaluation of the integral in Equation (7) is done by the residue theorem, using a contour consisting of a semicircle in the upper half of the complex  $\xi$  plane and the real axis.

For ideal bonding between the PWAS and the plate, the shear stress in the bonding layer and the corresponding space-domain Fourier transform are

$$\tau(x) = a\tau_0 [\delta(x-a) - \delta(x+a)], \quad \tilde{\tau} = a\tau_0 [-2i \sin \xi a] \quad (10)$$

Hence, the strain-wave solution becomes

$$\varepsilon_x(x, t) = -i \frac{a\tau_0}{\mu} \sum_{\xi^S} \sin \xi^S a \frac{N_S(\xi^S)}{D'_S(\xi^S)} e^{i(\xi^S x - \omega t)} - i \frac{a\tau_0}{\mu} \sum_{\xi^A} \sin \xi^A a \frac{N_A(\xi^A)}{D'_A(\xi^A)} e^{i(\xi^A x - \omega t)} \quad (11)$$

Similarly, the displacement wave solution is obtained as

$$u_x(x, t) = -i \frac{a\tau_0}{\mu} \sum_{\xi^S} \frac{\sin \xi^S a}{\xi^S} \frac{N_S(\xi^S)}{D'_S(\xi^S)} e^{i(\xi^S x - \omega t)} - i \frac{a\tau_0}{\mu} \sum_{\xi^A} \frac{\sin \xi^A a}{\xi^A} \frac{N_A(\xi^A)}{D'_A(\xi^A)} e^{i(\xi^A x - \omega t)} \quad (12)$$

A plot of these equations up to 1000 kHz is presented in Figure 6. Equations (11) and (12) contains the  $\sin \xi a$  behavior that displays maxima when the PWAS length  $l_a = 2a$  equals an odd multiple of the half wavelength, and minima when it equals an even multiple of the half wavelength. A complex pattern of such maxima and minima emerges, since several Lamb modes, each with its own different wavelength, coexist at the same time. Figure 6 shows the remarkable fact that, at 300 kHz, the amplitude of the  $A_0$  mode goes through zero, while that of the  $S_0$  is close to its peak. This represents an excitation ‘‘sweet spot’’ for  $S_0$  Lamb waves. Experimental results confirming this prediction are presented in Figure 6b.

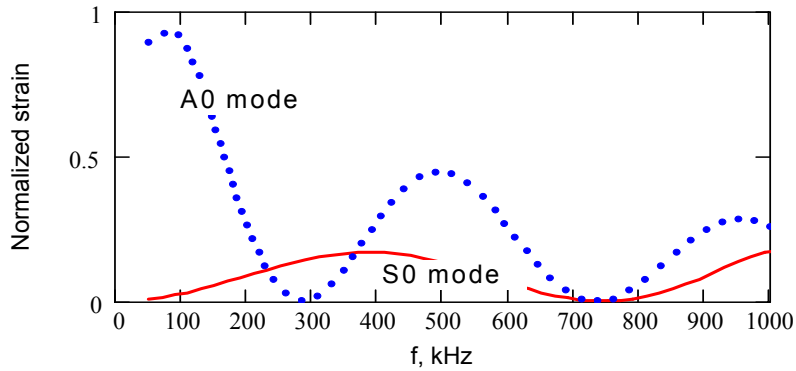
This proves that frequencies can be found for which the response is dominated by certain preferentially excited modes. This is **wavelength-based mode tuning**. Another factor that must be considered in Lamb wave tuning under PWAS excitation is the mode amplitude at the plate surface. This factor is contained in the values taken for each mode by the function  $N/D'$ . Hence, it is conceivable that, at a given frequency, some higher modes may have less surface amplitudes, while other may have larger surface amplitudes. Thus, two important factors have been identified for the design of PWAS-based Lamb-wave embedded NDE for structural health monitoring:

- a) The variation of  $|\sin \xi a|$  with frequency for each Lamb wave mode
- b) The variation of the surface strain with frequency for each Lamb wave mode

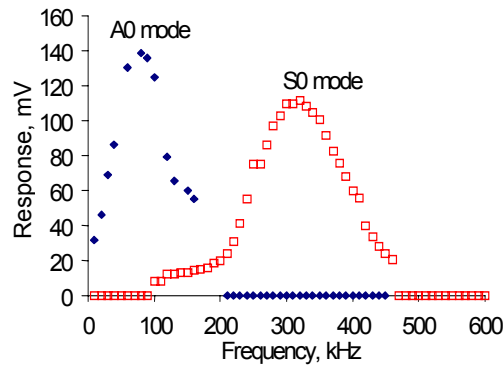
Equations (11) and (12) can be viewed as a superposition of waveguide Lamb modes. In this case, the contribution of each mode in these equations can be expressed in the general form

$$A_{\xi}(x,t) = G \cdot E_{\xi} \cdot F \cdot e^{i(\xi x - \omega t)} \quad (13)$$

where  $G$  is a numerical factor representing the PWAS *transducer power* transmitted to the structure,  $E_{\xi}$  is the *excitability function* of mode  $\xi$ , and  $F$  is the *Fourier transform of the excitation*.



(a)



(b)

**Figure 6** (a) Strain Lamb wave amplitudes predicted by the Lamb wave PWAS excitation tuning ( $S_0$  = continuous line;  $A_0$  = dotted line); (b) excitation “sweet spot” observed experimentally at 300 kHz in a 1.6-mm aluminum plate under a 7-mm PWAS excitation

## 6 Pulse-Echo Crack Detection with PWAS

Wave propagation experiments were conducted on an aircraft panel to illustrate crack detection through the pulse-echo method. The panel has a typical aircraft construction. It features a vertical splice joint and two horizontal stiffeners. Figure 7

shows three photographs of PWAS installation on increasingly more complex structural regions of the panel. Adjacent to the photographs are the PWAS signals. All the experiments used only one PWAS, operated in pulse-echo mode. The PWAS was placed in the same relative location, i.e., at 200 mm to the right of the vertical row of rivets. The first row of Figure 7 shows the situation with the lowest complexity, in which only the vertical row of rivets is present in the far left. The signal to the right of this photograph shows the initial bang (centered at around 5.3  $\mu$ s) and multiple reflections from the panel edges and the splice joint. The echoes start to arrive at approximately 60  $\mu$ s. The second row of Figure 7 shows the vertical row of rivets in the far left and, in addition, a horizontal double row of rivets stretching towards the PWAS. The signal to the right shows that, in addition to the multiple echoes from the panel edges and the splice, the PWAS also receives backscatter echoes from the rivets located at the beginning of the horizontal row. These backscatter echoes are visible at around 42  $\mu$ s. The third row in Figure 7 shows a region of the panel similar to that presented in the previous row, but having an addition feature: a simulated crack emanating from the first rivet hole in the top horizontal row. The simulated crack was a 12.7-mm hairline slit manufactured through electric discharge machining (EDM) method. The signal at the right of this photo shows features similar to those of the previous signal, but somehow stronger at the 42  $\mu$ s position. The features at 42  $\mu$ s correspond to the superposed reflections from the rivets and from the crack. The detection of the crack seems particularly difficult because the echoes from the crack and from the rivets are superposed.

This difficulty was resolved by using the differential signal method, i.e., subtracting the signal presented in the second row from the signal presented in the third row. In practice, such a situation would correspond to subtracting a signal previously recorded on the undamaged structure from the signal recorded now on the damaged structure. Such a situation of using archived signals is typical of health monitoring systems. When the two signals were subtracted, the result presented in the last row of Figure 7 was obtained. This differential signal shows a “loud and clear” echo due entirely to the crack. The echo, marked “reflection from the crack” is centered at 42  $\mu$ s, i.e.,  $\text{TOF} = 37 \mu\text{s}$  which correlates very well with a 5.4 km/s 200-mm total travel from the PWAS to the crack placed at 100 mm. The cleanness of the crack-detection feature and the quietness of the signal ahead of the crack-detection feature are remarkable. Thus, we concluded that PWAS are capable of clean and un-ambiguous detection of structural cracks.

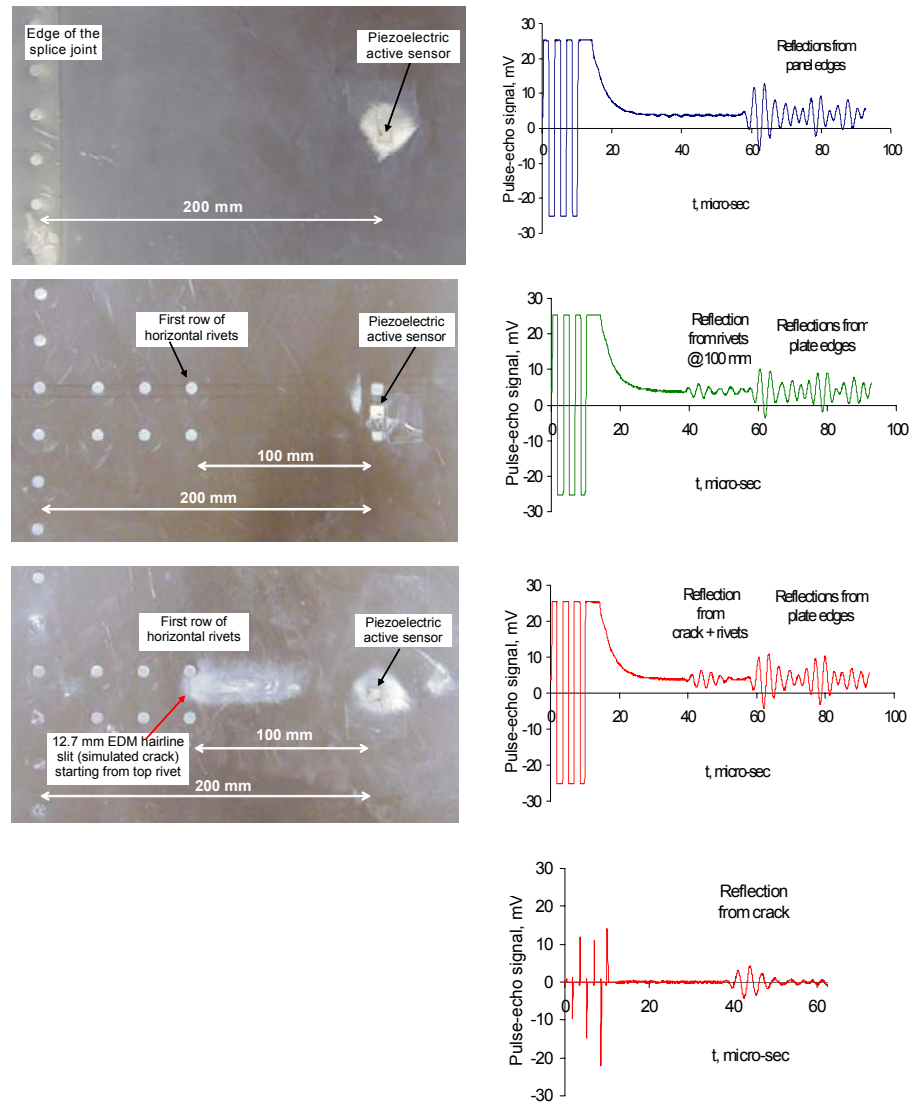


**Figure 7 Crack-detection laboratory experiments on an aircraft panel: left column represents specimens (40-mil 2025 T3) with increasing complexity. Right column represents the pulse-echo signals. Fourth picture in the right column shows the crack detection through the differential signal method**

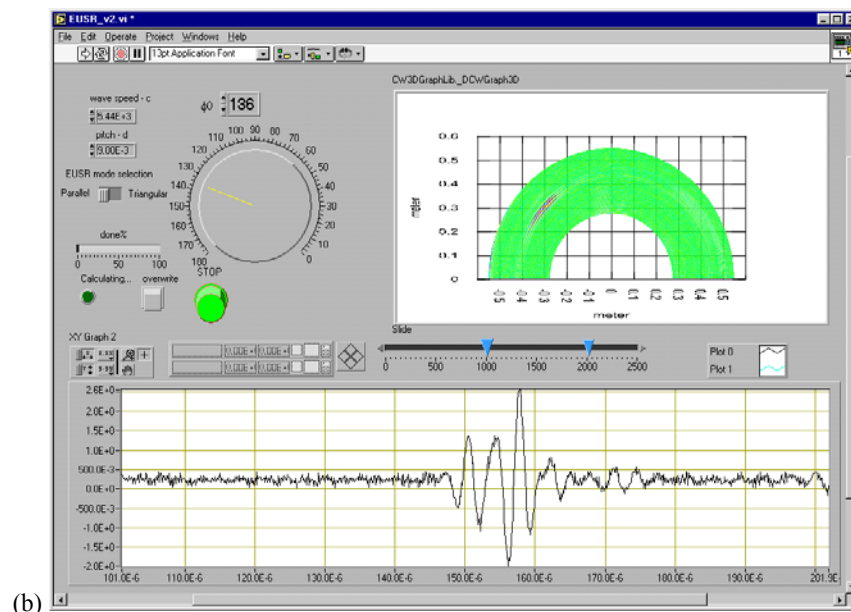
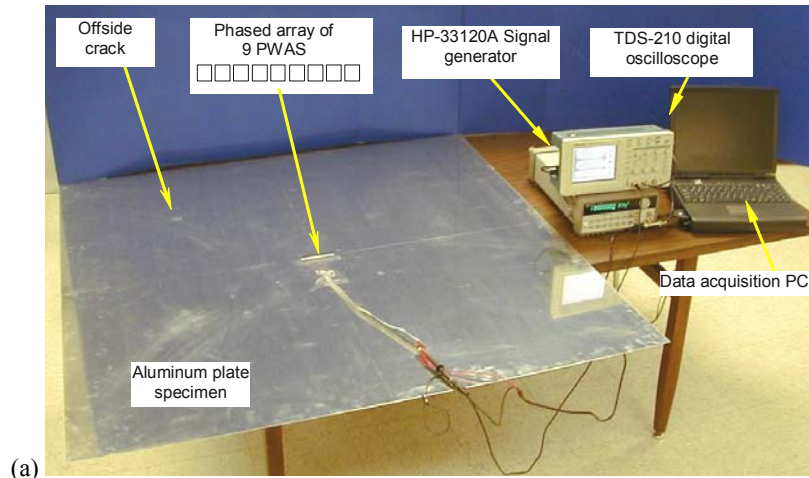


**Figure 8** Proof-of-concept EUSR experiment: (a) thin plate specimen 9-element PWAS array and 19-mm offside crack; (b) Graphical user interface (EUSR-GUI) front panel. The angle sweep is performed automatically to produce the structure/defect imaging picture on the right. Manual sweep of the beam angle can be also performed with the turn knob; the signal reconstructed at the particular beam angle (here,  $\phi_0 = 136$  deg) is shown in the lower picture

## 7 PWAS Phased Arrays

We have developed a PWAS phased array technology for thin wall structures (e.g., aircraft shells, storage tanks, large pipes, etc.) that uses Lamb waves to cover a large surface area through beam steering from a central location. We called this concept *embedded ultrasonics structural radar* (EUSR). A PWAS array was made up of a number of identical 7-mm sq. elements aligned at uniform 9-mm pitch (Figure 8a). The PWAS phased array was placed at the center of a 4-ft square thin aluminum plate. The wave pattern generated by the phased array is the result of the superposition of the waves generated by each individual element. By sequentially firing the individual elements of an array transducer at slightly different times, the ultrasonic wave front can be focused or steered in a specific direction. Thus, we achieved electronic sweeping and/or refocusing of the beam without physical manipulation of the transducers. We proved that inspection of a wide zone is possible by creating a sweeping beam of ultrasonic Lamb waves that covered the whole plate. Once the beam steering and focusing was established, the detection of crack was done with the pulse-echo method. During these proof-of-concept experiments, the EUSR methodology was used to detect cracks in two typical situations: (i) a 19-mm broadside crack placed at 305 mm from the array in the 90 deg direction; and (ii) a 19-mm broadside crack placed at 409 mm from the array in the 136 deg direction. Of these two, the latter was more challenging because the ultrasonic beam is not reflected back to the source but rather deflected sideways. Hence, the echo received from the offside crack is merely the backscatter signal generated at the crack tips. Figure 8b presents the front panel of the embedded ultrasonic structural radar graphical user interface (EUSR-GUI) displaying the offside signals. The sweep is performed automatically to produce the structural defect image in the right pane. Manual sweep can be performed with the turn knob. The reconstructed signal is shown in the lower pane. In Figure 8b, the lower pane show the signal reconstructed at the beam angle  $\phi_0 = 136$  deg corresponding to the crack location.

## 8 Electro-Mechanical Impedance Method for Damage Identification

The mechanical impedance method is a damage detection technique complementary to the wave propagation techniques. The principles of the E/M impedance technique are illustrated in Figure 9. The drive-point impedance presented by the structure to the active sensor can be expressed as the frequency dependent variable,  $Z_{str}(\omega) = k_{str}(\omega)/i\omega = k_e(\omega) - \omega^2 m(\omega) + i\omega c_e(\omega)$ . Through the mechanical coupling between the piezoelectric wafer active sensor (PWAS) and the host structure, on one hand, and through the electro-mechanical (E/M) transduction inside the PWAS, on the other hand, the drive-point structural impedance is reflected directly in the electrical impedance,  $Z(\omega)$ , at the active sensor terminals:

$$Z(\omega) = \left[ i\omega C \left( 1 - \kappa_{31}^2 \frac{\mathcal{Z}(\omega)}{1 + \mathcal{Z}(\omega)} \right) \right]^{-1}, \quad (14)$$

where  $C$  is the zero-load capacitance of the PWAS and  $\kappa_{31}$  is the electro-mechanical cross coupling coefficient of the PWAS ( $\kappa_{31} = d_{13} / \sqrt{s_{11} \epsilon_{33}}$ ), and  $\mathcal{Z}(\omega) =$

$k_{str}(\omega)/k_{PWAS}$ , with  $k_{PWAS}$  being the static stiffness of the PWAS. During a frequency sweep, the real part of the E/M impedance,  $Z(\omega)$ , follows the up and down variation as the structural impedance as it goes through the peaks and valleys of the structural resonances and anti-resonances (Giurgiutiu and Zagrai, 2002). The electro-mechanical impedance method is applied by scanning a predetermined frequency range in the high kHz band and recording the complex impedance spectrum. By comparing the real part of the impedance spectra taken at various times during the service life of a structure, meaningful information can be extracted pertinent to structural degradation and the appearance of incipient damage. On the other hand, analysis of the impedance spectrum supplies important information about the sensor integrity. The frequency range used in the E/M impedance method must be high enough for the signal wavelength to be significantly smaller than the defect size. From this point of view, the high-frequency E/M impedance method differs organically from the low-frequency modal analysis approaches.

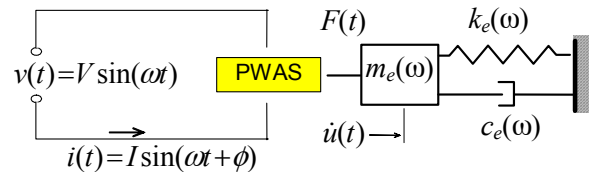


**Figure 9 Electro-mechanical coupling between piezoelectric active sensor and structure**

A series of experiments on thin-gage circular plates were conducted to validate and calibrate the E/M impedance technique (Giurgiutiu and Zagrai, 2001). Twenty-five aluminum plate specimens (100-mm diameter, 1.6-mm thick) were constructed from aircraft-grade aluminum stock. Each plate was instrumented with one 7-mm diameter PWAS placed at its center (Figure 10a). Damage detection experiments were conducted over three frequency bands: 10-40 kHz; 10-150 kHz, and 300-450 kHz. The data was process by analyzing the real part of the E/M impedance spectrum. A damage-metric was sought to quantify the difference between two spectra, “pristine” and “damaged”. Figure 10b indicates that the presence of the crack modifies the pointwise E/M impedance spectrum. Resonant frequency shifts and the appearance of new resonances are noticed. The closer the crack to the sensor, the more profound these changes are.

Several damage metrics were tried. These damage metrics fall into two large categories:

1. Overall statistics damage metrics
2. Neural network damage metrics

The following overall statistics damage metrics were considered in our analysis: root mean square deviation (RMSD); mean absolute percentage deviation (MAPD); covariance change (CC); correlation coefficient, R, deviation (CCD). The  $(1-R^2)^7$  damage metric applied to the 300-450 kHz band was found to decrease almost linearly with the distance between the crack and the sensor. However, in order to

obtain consistent results in general situations, the proper frequency band (usually in high kHz) and the appropriate damage metric must be used.

The neural networks approach to spectral damage metric was used in two steps. First, the spectral features were extracted such as to reduce the problem dimensionality from the 400 points used in the spectrum to just a few mechanical resonance features. This approach was used in the 10-40 kHz band. Feature vectors of size 4, 6, and 11 were used. Severe damage was detected easily, even with a small feature vector size. However, the slight damage required a feature vector of at least size 6 in order to attain consistent damage detection.

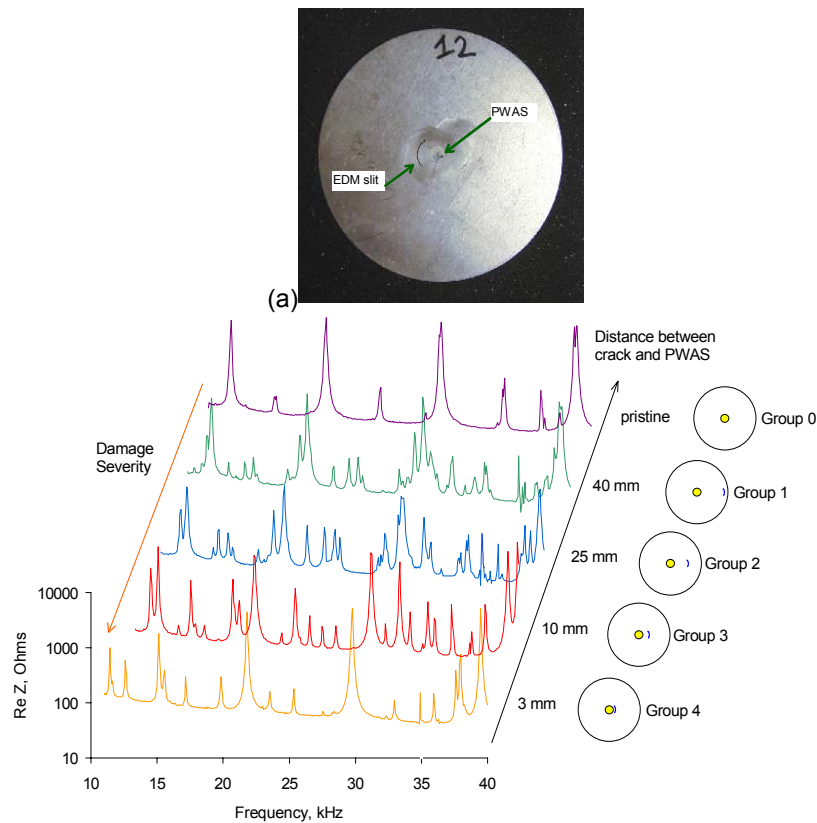


**Figure 10 (a) 100-mm diameter thin disc with a 7-mm PWAS at its center; (b) dependence of the E/M impedance spectra on the damage location**

### 9 Damage Identification in Aging Aircraft Panels

Realistic aircraft panels with structural details typical of metallic aircraft structures (rivets, splices, stiffeners, etc.) were also tested with the E/M impedance

technique. The specimens were made of 1 mm (0.040”) thick 2024-T3 Al-clad sheet assembled with 4.2 mm (0.166”) diameter countersunk rivets (Figure 11). Two specimens were considered: **Panel 0** and **Panel 1**. Panel 0 had two identical structural regions featuring a hidden stiffener held in place with two rows of rivets. Panel 1 had the same structural regions, only that it had, in addition, a 12.7 mm (0.5”) simulated crack originating from the first rivet hole of the lower region.

The panels were instrumented with **eight** PWAS, four on each panel. Based on the sensor distance from the crack location, we defined *medium field* (at ~100 mm from the crack) and *near field* (at ~10 mm from the crack). On each panel, two sensors were placed in the *medium field* (100 mm from the crack location), and two in the crack *near field* (10 mm from the crack location). It was anticipated that sensors placed in a similar configuration with respect to structural details (rivets, stiffeners, etc.) would give similar E/M impedance spectra. It was also anticipated that the presence of the simulated crack would only change the readings of the sensors in the affected region, and leave the other readings the same. According to Figure 11, sensors S1, S2, S3 are all in pristine medium field locations and should give similar readings. Similarly, sensors S5, S6, S7 are in pristine near field locations and, again, should give similar readings. Sensor S4 is in the medium field of the damage; it should give different readings than sensors S1, S2, S3. Similarly, sensor S8 is in the near field of the damage; it should give different reading than sensors S5, S6, S7.

The high frequency E/M impedance spectrum was collected for each sensor in the 200-550 kHz band, which shows a high density of resonance peaks. During the experiment, both aircraft panels were supported on foam to simulate free boundary conditions. The data was collected with HP 4194A impedance analyzer and then loaded into the PC through the GPIB interface.

### 9.1 Classification of Crack Damage in the PWAS Near-Field

The near field PWAS were S5, S6, S7, S8. Of these, S5, S6, S7 were in “pristine” situations, while S8 was in a “damaged” situation. Figure 12a shows the superposition of the spectra obtained from these sensors. Examination of these spectra reveals that sensor S8, placed next to the crack, has two distinct features that make it different from the other three spectra: (a) a higher-density of peaks; (b) an elevated dereverberated response in the 400-450 kHz range. On the other hand, the spectra of sensors S5, S6, S7 do not show significant differences among themselves. To quantify these observations, we used two methods:

- (i) Overall statistics metrics of the dereverberated response (DR)
- (ii) Probabilistic neural networks (PNN).

Figure 12b shows the DR curves extracted from the Figure 12a spectra. It is clear that the three DR’s for the “pristine” scenario (S5, S6, S7) are very similar. In contrast, the DR for the “damaged” scenario, S8, is clearly different. We used the overall-statistics damage metrics RMSD, MAPD, CCD to quantify the differences between the DR curves. The results of this analysis are presented graphically in Figure 12c. It is apparent that the CCD metric has the stronger detection capability.

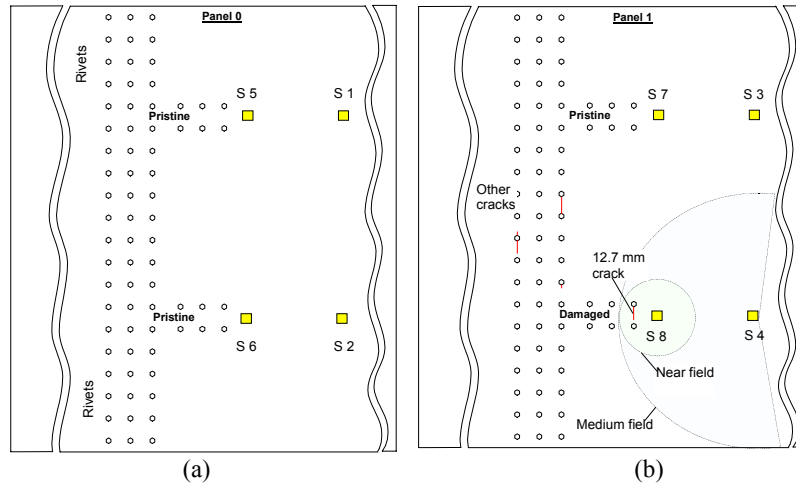


**Figure 11** Schematics of the aging aircraft panel specimens and PWAS configuration: (a) panel 0, sensors S1, S2, S5, S6; (b) panel 1, sensors S3, S4, S7, S8

### 9.2 Classification of Crack Damage in the PWAS Medium-Field

The medium field PWAS were S1, S2, S3, S4. Of these, S1, S2, S3 were in “pristine” situations, while S4 was in a “damaged” situation. The E/M impedance spectra for these sensors are presented in Figure 13. It is apparent that the spectra for S1, S2, S3 are consistently similar, while that for S4 is different. The S4 spectrum displays higher amplitudes of some of the spectral resonances in comparison with the spectra for S1, S2, S3. It also has new peaks. However, the changes due to damage in the medium field are much slighter than the changes observed in the near field. No change in the dereverberated response could be observed.

The use of overall statistics damage metrics on the near field spectra failed to give conclusive classification results. The reason for this situation is that the spectra dereverberated response is not significantly affected by medium field damage. To achieve classification of the medium-field spectra we used the PNN approach. First, a features extraction algorithm based on a search window and amplitude thresholds was applied. The 48 extracted features are shown graphically in Figure 13b,c. Then, the PNN algorithm was used to achieve the actual classification.

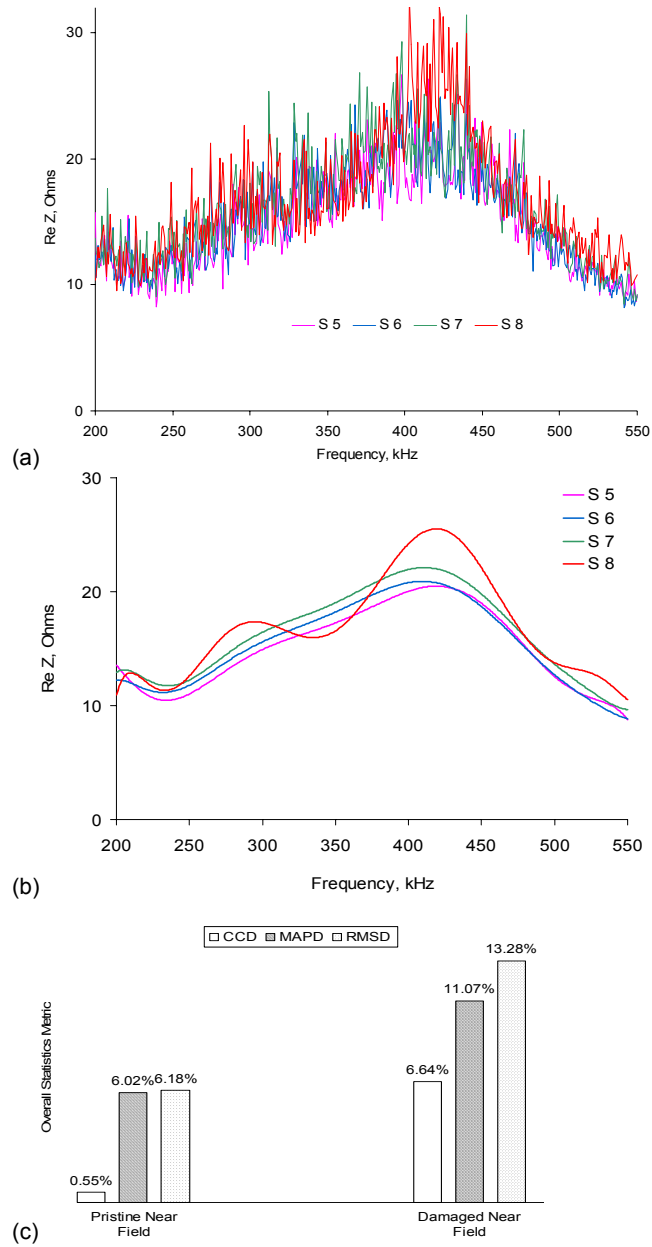


**Figure 12 PWAS E/M impedance near field damage detection: (a) superposed raw spectra; (b) dereverberated response; (c) overall-statistics damage metrics**

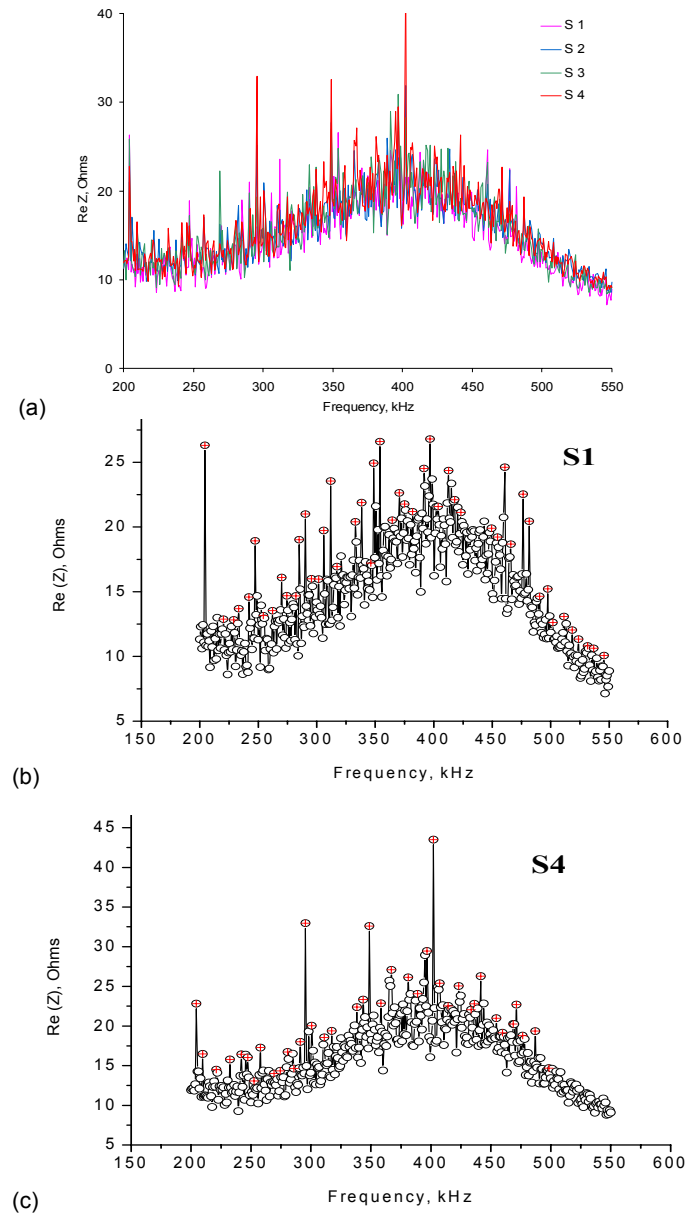


**Figure 13** Medium-field damage detection experiment with PWAS E/M impedance: (a) superposed raw spectra; (b) sensor S1 – “pristine” spectrum; (c) sensor S4 – “damaged” spectrum (the circled crosses represent the results of the feature extraction algorithm)

The resonance peaks picked by the feature extraction algorithm are marked with a cross in the data point. It can be seen that the resonance frequencies for the “pristine” and “damaged” scenarios are different. For example, the “pristine” scenario features several peaks above 500 kHz, while the “damaged” scenario does not show any peaks in this bandwidth. Because of this process, we were able to construct four feature vectors, each 48 long, which served as inputs to the PNN. Of these, three vectors represented “pristine” condition (S1, S2, S3) while the fourth vector represented a “damaged” condition (S4).

The PNN was designed to classify data into two classes: “pristine” and “damaged”. Since we had three “pristine” input vectors and one “damaged” input vector, we used one of three “pristine” input vectors for training, and the other three vectors (two “pristine” and one “damaged”) for validation. (No training was feasible for the “damaged” scenario). This created a dichotomous situation, in which the PNN would recognize data when it belongs to the “pristine” class and would reject it when it did not belong to the “pristine” class. The PNN was able to correctly classify data into the correspondent classes regardless of the choice of training vector for the “pristine” class. After successfully using the PNN method to detect damage in the medium field, we also used it for damage classification in the near field. We conclude that the aging aircraft classification problems for both medium field and near field can be successfully addressed with the PNN algorithm.

An additional note regarding the localization property of the E/M impedance method is worth making. Panel 1 had several other simulated cracks besides those discussed here. However, these cracks were away from the PWAS, and hence outside their sensing range. For this reason, these other cracks did not noticeable influence the sensors readings. The localization property of the E/M impedance method is important for finding the approximate location of the damage on the structure.

### Impact Detection with Piezoelectric Wafer Active Sensors

Impact detection with piezoelectric wafer active sensors in composite materials was successfully demonstrated by Wang and Chang (2000), Dupont *et al.* (2000), and others. In our experiments, the array of piezoelectric wafer active sensors was also used to detect low-velocity foreign object impact on metallic aircraft-grade aluminum plates. In our experiments, we used a small steel ball (0.16 g) dropped from a height of 50 mm. Figure 14b presents the signals recorded on sensors # 1, #5, #7, #9. The corresponding signal time of flight (TOF) values are  $t_1 = 0.1070$  ms,  $t_5 = 0.1560$  ms,  $t_7 = -0.0312$  ms,  $t_9 = 0.1800$  ms, relative to the oscilloscope trigger. Figure 14b shows the straight-line fit through the distance-TOF points. The top line represents the raw data: a group velocity of  $c = 1.6058$  km/s is determined from the straight-line gradient (99.86% correlation). This group velocity is consistent with the predicted  $A_0$  group velocity value corresponding to basic signal frequency of 45 kHz. The bottom line of Figure 14c represents the distance-TOF correlation obtained after the TOF was adjusted for the oscilloscope trigger response ( $\Delta\text{TOF} = 73$  micro-sec). This line passes through the origin, as expected.

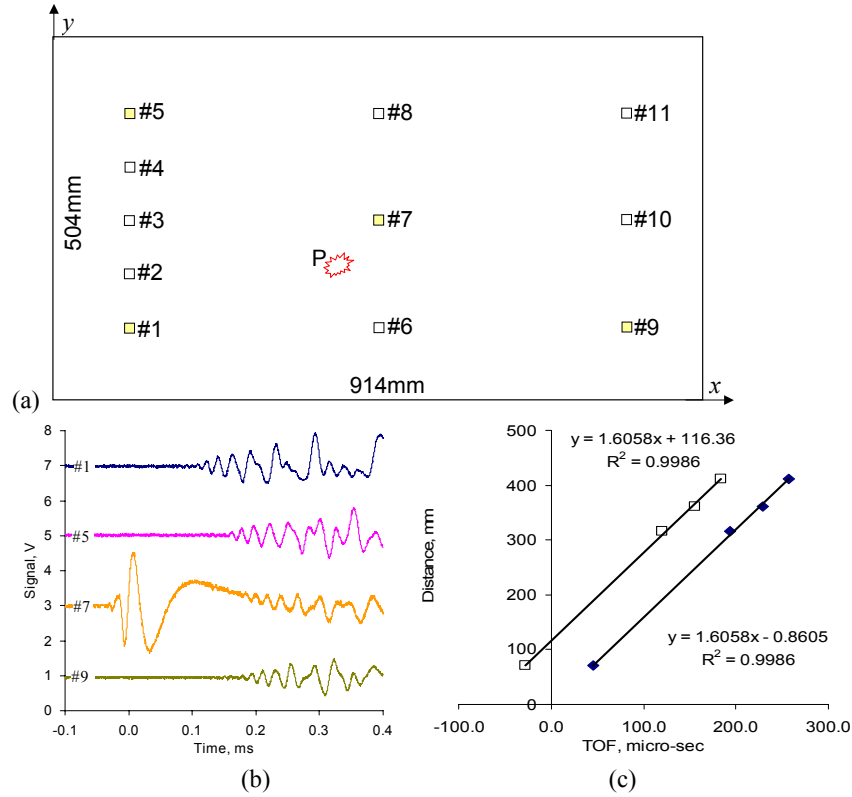


**Figure 14 Impact detection (ID) experiments: (a) location of impact and sensors (b) captured ID signals with arbitrary time origin due to oscilloscope trigger; (c) straight-line fit of the distance-TOF values (top = raw time data; bottom = adjusted for oscilloscope trigger). The ID event was a 0.16 g steel-ball dropped from a 50 mm height; the locations of the sensors and of the event are given in Table 1**

The distance and TOF data used to detect the impact position are given in Table 1. Assuming the unknown impact position is  $(x, y)$ , the following set of simultaneous nonlinear equations represent the correlation between distance, group velocity and TOF

$$(x_i - x)^2 + (y_i - y)^2 = (c \cdot t_i)^2, \quad i = 1, \dots, 4 \quad (15)$$

These equations represent an over-constrained set of equations (four equations, two unknowns), which can be solved using error minimization routines. In our studies, we tried two methods: (a) global error minimization; and (b) individual error minimization. It was found that individual error minimization gave marginally better results. The impact location determined by these calculations was  $x_{\text{impact}} = 400.7$  mm,

$y_{\text{impact}} = 187.5$  mm. These values are within 0.2% and 6.2%, respectively, of the actual impact location (400 mm and 200 mm).

**Table 1** Position of sensors ( $x$ ,  $y$ ) and their radial distance,  $r$ , from the acoustic emission (AE) and impact detection (ID) events. (The TOF was adjusted by 73 micro-sec to account for Oscilloscope trigger effects.)

Sensor	Distance, mm			TOF for ID, micro-sec	
	x	y	r	Raw	Adjusted
#1	100	100	316	120	193
#5	100	400	361	156	229
#7	450	250	71	-31	42
#9	800	100	412	180	253
AE/ID event	400	200	0	N/A	N/A

These experiments have proven that the piezoelectric-wafer active sensors are capable of detecting low-velocity impact signals. The high sensitivity of these sensors is remarkable since signals of up to  $\pm 1.5$  V were directly recorded without the need for any signal conditioning/pre-amplifiers. It was also shown how data processing algorithms could determine the impact location with reasonable accuracy.

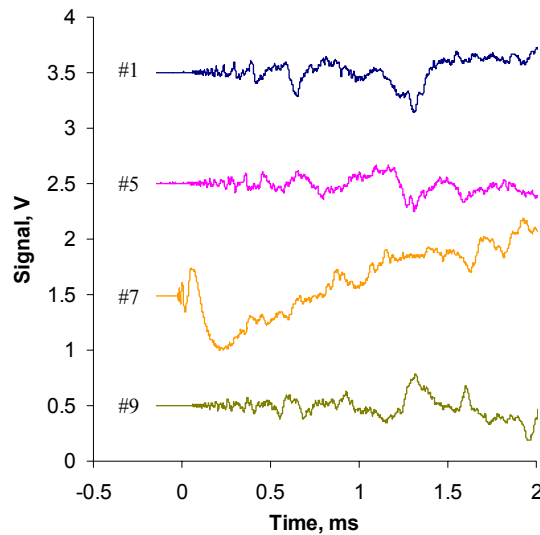


**Figure 15** PWAS captured acoustic emission (AE) signals from a simulated AE event (coordinate locations are given in Table 1)

### Acoustic Emission Detection with Piezoelectric Wafer Active Sensors

Historically, acoustic emission signals have been captured with special-purpose acoustic emission sensors (e.g., Ikegami and Haugse, 2001; Mal, 2001; Dzenis and Qian, 2001), which are costly and obtrusive. Blanas *et al.* (1997) and Dupont *et al.* (2000) studied the possibility of using embedded piezoelectric wafer sensors to detect acoustic emission signals in composite materials. To illustrate the capability of piezoelectric wafer active sensors to detect acoustic emission signals in metallic materials, we performed detection experiments on the rectangular plate specimen, which was already instrumented with an array of PWAS. Acoustic emission (AE) events were simulated at the location P,  $x_P = 400$  mm,  $y_P = 200$  mm (Figure 14a). Table 1 shows the location of the sensors and their radial distance from the AE event. Consistent with other investigators, (e.g., Blanas, 1997; Dzenis and Qian, 2001), the acoustic emission events were simulated by pencil lead breaks on the specimen surface (0.5 mm HB leads).

The simulated acoustic emission signals captured at sensors #1, #5, #7, #9 are shown in Figure 15 (for display, the signals were spaced up by vertical shifts). The signal on sensor #7, closest to the AE source ( $r_7 = 71$  mm), is the strongest. This signal displays both high frequency and low-frequency components, corresponding to  $S_0$  (axial) and  $A_0$  (flexural) waves, respectively. The flexural ( $A_0$ ) waves display much higher amplitudes than the axial ( $S_0$ ) waves, though their travel speed is slower. The signals received at the other sensors display similar trends, though of lower amplitudes, due to their greater distance from the AE source. These experiments have proven that the piezoelectric-wafer active sensors are capable of detecting AE signals. The high sensitivity of these sensors is remarkable since signals of up to  $\pm 0.5$  V were directly recorded without the need for any signal conditioning/pre-amplifiers.

### 10 PWAS Rayleigh Waves NDE in Rail Tracks

In order to test the feasibility of transmitting and receiving Rayleigh waves with PWAS technology in massive structures, we conducted a small-scale demonstration experiment on a rail track specimen (Figure 16). A 5-ft piece of rail was instrumented with 5 piezoelectric wafer active sensors (PWAS). Each PWAS consists of a 7-mm square piezoelectric wafer (0.2 mm thin) affixed to the rail surface. Ultrasonic waves in the 300 kHz band were generated at one end of the rail specimen and received at the other end, as well as at intermediate locations. Figure 16c shows the waves transmitted from one sensor and received at other two sensors. These waves are *surface-guided waves* (Rayleigh waves) and can travel a long distance in the rail with very little attenuation. Figure 16c indicates that the time of flight (TOF) is directly proportional with distance. Rayleigh wave speed can be predicted with the expression  $c_R = \sqrt{G/\rho} (0.87 + 1.12\nu)/(1 + \nu)$  where  $G$  is the shear modulus of the material, and  $\rho$  the specific mass. For carbon steels,  $c_R = 2.9$  km/s. Figure 16d shows the plot of distance vs. time predicted by this formula, and the two experimental points corresponding to sensors 1 and 2. The correlation between theory and experiment is very good, which gives confidence in our

proposed concept. If cracks were present, reflections would be received. When corrosion is present, the wave speed changes. The detection of crack will be examined under the proposed effort.

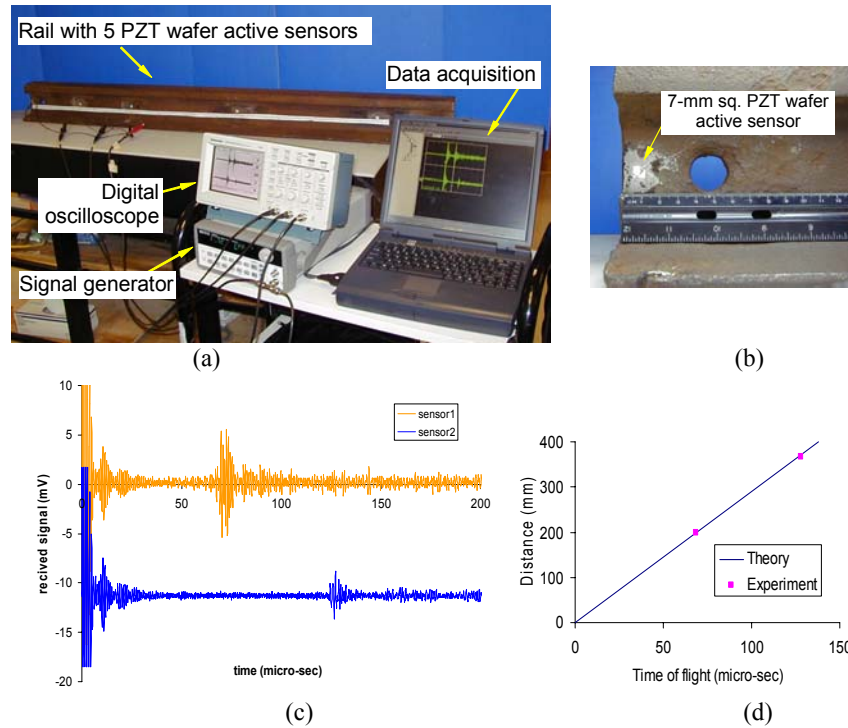


**Figure 16** Transmission and reception of surface-guided Rayleigh wave with PWAS in a rail track specimen: (a) track rail specimen with 5 active sensors and lab instrumentation; (b) details of one sensor installation; (c) surface-guided Rayleigh waves received at 200 mm (sensor 1) and 365 mm (sensor 2); (d) plot of distance vs. time.

The PWAS Rayleigh wave concept is completely *non-intrusive*, since the ultrasonic guided waves are generated with surface mounted transducers that can be retrofitted to existing rails without any disruption to the rail traffic. In contrast, conventional axial-waves ultrasonic transducers would have to be incorporated into the rail, which is not feasible. The proposed concept is *robust*, since the ultra-thin piezoelectric wafers present a very low profile and can be easily protected. In contrast, conventional ultrasonic surface-wave ultrasonic transducers are bulky and obtrusive, since they require an intermediate coupling wedge to attain axial-to-surface mode conversion. The proposed concept is inexpensive, since the PWAS transducers currently cost around \$7, while conventional ultrasonic transducers cost hundreds of dollars, i.e., two orders of magnitude more.

## 11 Conclusion

This paper has presented the use of piezoelectric wafer active sensors (PWAS) for embedded ultrasonic nondestructive evaluation (NDE). Recent trends in guided-wave ultrasonic NDE and damage identification were briefly reviewed. Opportunities for the PWAS sensors as embedded transmitters and receiver of guided Lamb and Rayleigh waves were identified. The PWAS were briefly described along with their principle of operation. The interaction between PWAS and ultrasonic Lamb waves was modeled and analyzed. Excitation “sweet spots” for preferentially exciting certain Lamb wave modes were identified. Then, the use of PWAS for embedded pulse-echo detection of structural cracks was exemplified. PWAS phased arrays were used in conjunction with the embedded ultrasonics structural radar (EUSR) algorithm to create scanning Lamb wave beams for large area interrogation. For local area interrogation, the use of PWAS in conjunction with the electromechanical (E/M) impedance method was discussed in the context of a standing wave NDE technique. Examples of local area crack detection in circular plates and aircraft panels were provided. Spectral classification methods based on overall statistics and neural networks were discussed. Passive PWAS usage for acoustic emission and impact detection was presented. The use of PWAS for Rayleigh wave ultrasonics was also illustrated.

Since the embedded ultrasonic NDE with piezoelectric wafer active sensors is intended for structural health monitoring, an approximate location of the damage would be sufficient as a first alert. Once structural damage was identified in a certain area, further examination of the exact damage location and of its severity would be the object of detailed NDE investigations. These detailed NDE investigations would be initiated once the vehicle was pulled out of service due to structural health deficiency as signaled by the structural health monitoring equipment. Thus, the PWAS technology offers the necessary combination between low cost and lightweight, on one hand, and ultrasonic detection capabilities, on the other hand, to permit large area deployment in a whole structure. The PWAS are the enabling technology for the implementation of large area of structural health monitoring and embedded NDE concepts.

## 12 Acknowledgments

Financial support of National Science Foundation (CMS-9908293 and INT-9904493), US Air Force Research Laboratory (03-S470-033-C1/F33615-01-D-5801), and Sandia National Labs (BF 0133) is thankfully acknowledged.

## 13 References

- Alleyne, D. N.; Cawley P. (1992) “Optimization of Lamb Wave Inspection Techniques”, *NDT&E International*, Vol. 25 (1992), No. 1, pp. 11–22
- Alleyne, D. N., Pavlakovic, B., Lowe, M. J. S., Cawley, P. (2001) "Rapid, Long Range Inspection of Chemical Plant Pipework Using Guided Waves," *Review of Progress in*

- QNDE*, Vol. 20, (2001), pp. 180-187
- Banks, H. T., Smith, R. C., Wang, Y., (1996) "Smart Material Structures: Modeling, Estimation and Control", Masson, John Wiley & Sons, Paris 1996.
- Blanas, P., Wenger, M. P., Shuford, R. J., Das-Gupta, D. K. (1997) "Active Composite Materials and Damage Monitoring", *Proceedings of the International Workshop on Structural Health Monitoring*, Stanford University, CA, September 18-20, 1997, pp. 199-207.
- Chahbaz A., Gauthier J.; Brassard, M.; Hay, D. R. (1999) " Ultrasonic Technique for Hidden Corrosion Detection in Aircraft Wing Skin"; *Proceedings of the 3<sup>rd</sup> Joint Conference on Aging Aircraft, 1999*
- Chang, F.-K. (1995) "Built-In Damage Diagnostics for Composite Structures", in *Proceedings of the 10<sup>th</sup> International Conference on Composite Structures (ICCM-10)*, Vol. 5, Whistler, B. C., Canada, August 14-18, 1995, pp.283-289
- Chang, F.-K. (1998) "Manufacturing and Design of Built-in Diagnostics for Composite Structures", *52<sup>nd</sup> Meeting of the Society for Machinery Failure Prevention Technology*, Virginia Beach, VA, March 30 – April 3, 1998.
- Chang, F.-K. (2001) "Structural Health Monitoring: Aerospace Assessment", *Aero Mat 2001, 12th ASM Annual Advanced Aerospace Materials and Processes Conference*, 12-13 June 2001, Long Beach CA.
- Chaudhry, Z., Joseph, T., Sun, F., and Rogers, C. (1995) "Local-Area Health Monitoring of Aircraft via Piezoelectric Actuator/Sensor Patches," *Proceedings, SPIE North American Conference on Smart Structures and Materials*, San Diego, CA, 26 Feb. - 3 March, 1995; Vol. 2443, pp. 268-276.
- Crawley, E. A. and deLuis, J., (1987) "Use of Piezoelectric Actuators as Elements of Intelligent Structures", *AIAA Journal*, Vol. 25, No. 10, pp. 1375-1385, 1987.
- Culshaw, B.; Pierce, S. G.; Staszekski, N. J. (1998) "Condition Monitoring in Composite Materials: an Integrated System Approach", *Proceedings of the Institute of Mechanical Engineers*, Vol. 212, Part I, pp. 189-202
- Dalton, R. P.; Cawley, P.; Lowe, M. J. S. (2001) "The Potential of Guided Waves for Monitoring Large Areas of Metallic Aircraft Structure", *Journal of Nondestructive Evaluation*, Vol. 20, pp. 29-46, 2001
- De Villa, F.; Roldan, E.; Tirano, C.; Mares, R.; Nazarian, S.; Osegueda, R. (2001) "Defect Detection in Thin Plates Using  $S_0$  Lamb Wave Scanning", *Proceeding of SPIE Conference on Advanced Nondestructive Evaluation for Structural and Biological Health Monitoring*, March 6-8, 2001, Newport Beach, CA. Vol. 4335, p121-130
- Diamanti, K.; Hodgkinson, J. M.; Soutis, C. (2002) "Damage Detection of Composite Laminates Using PZT Generated Lamb Waves", *Structural Health Monitoring 2002*, Daniel Balageas (Ed.), DEStech Publications Inc., pp. 398-405
- Duke, J. C. Jr. (1988) *Acousto-Ultrasonics – Theory and Applications*, Plenum Press
- Dupont, M.; Osmont, R.; Gouyon, R.; Balageas, D. L. (2000) "Permanent Monitoring of Damage Impacts by a Piezoelectric Sensor Based Integrated System", in *Structural Health Monitoring 2000*, Fu-Kuo Chang (Ed.), Technomic, 2000, pp. 561-570.
- Dzenis, Y.; Qian, J. (2001) "Analysis of Microdamage Evolution Histories in Composites", *7<sup>th</sup> ASME NDE Topical Conference*, San Antonio, TX, April 23-25, 2001
- Fuller, C. R.; Snyder, S. D. Hansen, C. H.; Silcox, R. J. (1990), "Active Control of Interior Noise in Model Aircraft Fuselages Using Piezoceramic Actuators", American Institute of

Aeronautics and Astronautics Paper # 90-3922

- Giurgiutiu, V., and Rogers, C. A., (1997) "Electro-mechanical (E/M) impedance method for structural health monitoring and non-destructive evaluation", *International Workshop on Structural Health Monitoring, Stanford University, CA*, September 18-20, 1997, pp. 433-444.
- Giurgiutiu, V., Reynolds, A., and Rogers, C. A., (1998), "Experimental Investigation of E/M Impedance Health Monitoring of Spot-Welded Structural Joints" *Journal of Intelligent Material Systems and Structures*, Technomic Pub., USA, Vol. 10, No. 10, Oct. 1999, pp. 802-812
- Giurgiutiu, V., Zagrai, A. N. (2002) "Embedded Self-Sensing Piezoelectric Active Sensors for On-line Structural Identification", *Transactions of ASME, Journal of Vibration and Acoustics*, January 2001, Vol.124, pp. 116-125
- Giurgiutiu, V.; Zagrai, A. N.; Bao, J. (2002) "Embedded Active Sensors for In-Situ Structural Health Monitoring of Thin-Wall Structures", *ASME Journal of Pressure Vessel Technology*, Vol. 124, No. 3, August 2002, pp. 293-302
- Grondel, S.; Moulin, E.; Delebarre, C. (1999) "Lamb Wave Assessment of Fatigue Damage in Aluminum Plates", *Proceedings of the 3<sup>rd</sup> Joint Conference on Aging Aircraft, 1999*
- Krautkramer (1998) "Emerging Technology – Guided Wave Ultrasonics", *NDTnet*, Vol. 3, No. 6, June 1998
- IEEE Standard on Piezoelectricity, (1987), *An American National Standard*, The Institute of Electrical and Electronics Engineers, Inc., 1987.
- Ihn, J.-B.; Chang, F.-K. (2002) "Built-in Diagnostics for Monitoring Crack Growth in Aircraft Structures", *Proceedings of the SPIE 9<sup>th</sup> International Symposium on Smart Structures and Materials*, 17-21 March 2002, San Diego, CA, paper #4702-04
- Ikegami, R., and Haugse, E. D. (2001) "Structural health management for aging aircraft", *Proceedings of SPIE Industrial and Commercial Applications of Smart Structures Technologies*, Vol. 4332, p60-67
- Lakshmanan, K. A. and Pines, D. J. (1997) "Modeling Damage in Composite Rotorcraft Flexbeams Using Wave Mechanics", *Journal of Smart Materials and Structures* Vol. 6, No. 3, June, 1997, IOP, Bristol, England, p 383-392
- Lester, H. C.; Lefebvre, S. (1993) "Piezoelectric Actuator Models for Active Sound and Vibration Control of Cylinders", *Journal of Smart Materials and Structures*, Vol. 4, July 1993, pp. 295-306.
- Liang, C., Sun, F. P., and Rogers C. A. (1994) "Coupled Electro-Mechanical Analysis of Adaptive Material System-Determination of the Actuator Power Consumption and System energy Transfer", *Journal of Intelligent Material Systems and Structures*, Vol. 5, January 1994, pp. 12-20
- Light, G. M., Minachi, A., and Spinks, R. L. (2001) "Development of a Guided Wave Technique to Detect Defects in Thin Steel Plates Prior to Stamping", *Proceeding of the 7<sup>th</sup> ASME NDE Topical Conference*, NDE-Vol. 20, p163-165
- Lin, X; Yuan, F. G. (2001) "Damage Detection of a Plate using Migration Technique", *Journal of Intelligent Material Systems and Structures*, Vol. 12, No. 7, July 2001
- Mal, A. (2001) "NDE for Health Monitoring of Aircraft and Aerospace Structures", *Proceeding of the 7<sup>th</sup> ASME NDE Topical Conference*, NDE-Vol. 20, p149-155
- Mustafa V.; Chahbaz A. (1997) "Imaging of Disbond in Adhesive Joints with Lamb Waves"; *NDTnet* - March 1997, Vol.2 No.03 <http://www.ndt.net/article/tektren2/tektren2.htm>

- Osmont, D.; Dupont, M.; Gouyon, R.; Lemistre, M.; Balageas, D. (2000) "Damage and Damaging Impact Monitoring by PZT Sensors-based HUMS", *Proceedings of the SPIE Smart Structures and Materials 2000: Sensory Phenomena and Measurement Instrumentation for Smart Structures and Materials*, SPIE Vol. 3986, pp. 85-92
- Park, G., and Inman, D. J. (2001) "Impedance-based Structural Health Monitoring", Monograph: Nondestructive Testing and Evaluation Methods for Infrastructure Condition Assessment, edited by Woo, S.C., Kluwer Academic Pub., New York, NY.
- Rose, J. L. (1995) "Recent Advances in Guided Wave NDE", *1995 IEEE Ultrasonics Symposium*, pp. 761-770
- Rose, J. L.; Rajana, K. M.; Hansch, M. K. T. (1995) "Ultrasonic Guided Waves for NDE of Adhesively Bonded Structures", *Journal of Adhesion*, 1995, Vol. 50, pp. 71-82
- Rose, J. L. (1999) *Ultrasonic Waves in Solid Media*, Cambridge University Press, 1999
- Rose, J. L. (2002) "A Baseline and Vision of Ultrasonic Guided Wave Inspection Potential", *ASME Journal of Pressure Vessel Technology – Special Issue on Nondestructive Characterization of Structural Materials*, Vol. 124, No. 3, August 2002, pp. 273-282
- Singher, L.; Segal, Y.; Shamir, J. (1997) "Interaction of a Guided Wave with a Nonuniform Adhesion Bond", *Ultrasonics*, Vol. 35, 1997, pp. 385-391
- Sun, F. P., Liang C., and Rogers, C. A., (1994) "Experimental Modal Testing Using Piezoceramic Patches as Collocated Sensors-Actuators", *Proceeding of the 1994 SEM Spring Conference & Exhibits*, Baltimore, MI, June 6-8, 1994.
- Thomson, D. O. and Chimenti, D. E. (Editors) (2002) Review of Progress in Quantitative Nondestructive Evaluation, Chapter 2C "Guided Waves" and Chapter 7 "NDE Applications", *AIP Conference Proceedings* Vol. 615, 2002
- Todd, P. D.; Challis, R. E. (1999) "Quantitative Classification of Adhesive Bondline Dimensions Using Lamb Waves and Artificial Neural Networks", *IEEE Transactions of Ultrasonics, Ferroelectrics, and Frequency Control*, Vol. 46, No. 1, January 1999, pp. 167-181
- Tzou, H. S.; Tseng, C. I. (1990) "Distributed Piezoelectric Sensor/Actuator Design for Dynamic Measurement/Control of Distributed Parametric Systems: A Piezoelectric Finite Element Approach", *Journal of Sound and Vibration*, No. 138, pp. 17-34, 1990.
- Viktorov, I. A. (1967) "Rayleigh and Lamb Waves: Physical Theory and Applications", Plenum Press, 1967
- Wang, C. S.; Chang, F.-K. (2000) "Built-In Diagnostics for Impact Damage Identification of Composite Structures", in *Structural Health Monitoring 2000*, Fu-Kuo Chang (Ed.), Technomic, 2000, pp. 612-621